REPORT

BIOSYNTHESIS

Mapping the catalytic conformations of an assembly-line polyketide synthase module

Dillon P. Cogan[1]†, Kaiming Zhang[2,3]†, Xiuyuan Li[1], Shanshan Li[2,3], Grigore D. Pintilie[2], Soung-Hun Roh[2,4], Charles S. Craik[5], Wah Chiu[2,6]*, Chaitan Khosla[1,7,8]*

Assembly-line polyketide synthases, such as the 6-deoxyerythronolide B synthase (DEBS), are large enzyme factories prized for their ability to produce specific and complex polyketide products. By channeling protein-tethered substrates across multiple active sites in a defined linear sequence, these enzymes facilitate programmed small-molecule syntheses that could theoretically be harnessed to access countless polyketide product structures. Using cryogenic electron microscopy to study DEBS module 1, we present a structural model describing this substrate-channeling phenomenon. Our 3.2- to 4.3-angstrom-resolution structures of the intact module reveal key domain-domain interfaces and highlight an unexpected module asymmetry. We also present the structure of a product-bound module that shines light on a recently described "turnstile" mechanism for transient gating of active sites along the assembly line.

Polyketide synthases (PKSs) are multifunctional enzymes that synthesize numerous complex polyketides in nature. Mining of microbial and metazoan genomes continues to add to the surplus of untapped and potentially bioactive polyketide products and hybrids thereof. Among the small fraction (<5%) of characterized polyketides and their derivatives, some important medicines (*1*) and agrochemicals (*2*) have emerged. Many PKSs are composed of multiple homodimeric modules that individually catalyze C–C bond formation and optional modification of elongated intermediates. Such multimodular PKS arrays operate as enzymatic assembly lines by orchestrating the transfer of intermediates across modules in an ordered linear sequence. An example of a prototypical assembly-line PKS is the 6-deoxyerythronolide B synthase (DEBS) from *Saccharopolyspora erythraea* (Fig. 1) (*3*, *4*). A representative catalytic cycle of the first module of this assembly line is described in fig. S1.

[1]Department of Chemistry, Stanford University, Stanford, CA 94305, USA. [2]Department of Bioengineering, Stanford University, Stanford, CA 94305, USA. [3]MOE Key Laboratory for Cellular Dynamics, Hefei National Laboratory for Physical Sciences at the Microscale and School of Life Sciences, University of Science and Technology of China, Hefei, Anhui 230027, China. [4]Department of Biological Sciences, Institute of Molecular Biology & Genetics, Seoul National University, Seoul 151-742, Korea. [5]Department of Pharmaceutical Chemistry, University of California–San Francisco, San Francisco, CA 94158, USA. [6]Division of CryoEM and Bioimaging, Stanford Synchrotron Radiation Lightsource, SLAC National Accelerator Laboratory, Stanford University, Menlo Park, CA 94025, USA. [7]Department of Chemical Engineering, Stanford University, Stanford, CA 94305, USA. [8]Stanford ChEM-H, Stanford, CA 94305, USA.
*Corresponding author. Email: khosla@stanford.edu (C.K.); wahc@stanford.edu (W.C.)
†These authors contributed equally to this work.

Given the homodimeric nature of assembly-line PKSs, we had previously sought to trace, through functional analysis of hybrid DEBS proteins, the trajectory of a growing polyketide chain as it is channeled from one covalently bound state to the next (*5*). Our data led to a model in which polyketide translocation occurred through acyl carrier protein (ACP) → ketosynthase (KS) substrate channeling within the same subunit (intramolecularly), and chain elongation occurred through KS→ACP substrate channeling across subunits (intermolecularly). In the present work, we used single-particle cryogenic electron microscopy (cryo-EM) to structurally validate this long-standing model for substrate channeling.

We present near-atomic-resolution structures of DEBS module 1 (M1, 3.2 to 4.3 Å) with backbone and side-chain resolvability in each of the relevant catalytic domains, including the ACP. In addition to validating the substrate-channeling model (Fig. 1), these structures shine light on hitherto uncharacterized domain-domain interfaces. Perhaps most unexpectedly, they also reveal module asymmetry not observed in previous structures of intact PKS modules (*6*–*9*). To further characterize a recently discovered "turnstile" mechanism (*10*), we also report the cryo-EM structure of DEBS M1 in its putatively *turnstile-closed* state, corresponding to the product-bound module. The resulting structure offers a plausible basis for KS active site shielding and vectorial biosynthesis by PKS assembly lines.

In preparation for structural analysis, we adapted a previous protocol for buffer optimization by using protein melt-curve analysis paired with catalytic activity measurements (described in the materials and methods) (*11*). DEBS M1 and M3 fused to the C-terminal thioesterase (TE) domain were selected as model specimens, given the extensive catalytic (*12*–*14*) and structural (*15*–*18*) characterization of M3 and the ease of access to the substrates of M1. The addition of citrate to the buffer elevated thermostability, catalytic activity, and oligomeric uniformity (figs. S2 to S6), so we used it as an additive for single-particle cryo-EM analysis. In addition to small-molecule buffer additives, antigen-binding fragments (Fabs) of antibodies can be used as tags (*19*, *20*) to augment the sample rigidity for high-resolution structure determination. Our initial target module was a recently characterized hybrid DEBS module, M3/1, comprising fragments from M3 and M1 fused to the TE domain (i.e., KS3-AT3-KR1-ACP1-TE) (*21*), because all of its catalytic domains have been previously crystallographically characterized at atomic resolution (*15*–*17*, *22*). M3/1 was complexed with a noninhibitory Fab (1B2) that is specific for the N-terminal docking domain (*15*) and purified in a buffer containing 100 mM citrate. The Fab-free module was also prepared under otherwise identical conditions (fig. S7). Combined with grid-freezing parameter optimization, diagnostic cryo-EM micrographs of the vitrified samples revealed Fab-bound modules to have markedly improved particle quality compared with Fab-free modules. This effect is likely exerted by the conformational selectivity of Fab 1B2 for modules in the dimeric state, because we previously measured numerous contacts between individual Fabs and each of the modular subunits at the dimeric interface (*15*). Substantiating the utility of this Fab, a companion study also used it to successfully study a PKS module from the lasalocid assembly line by single-particle cryo-EM (*23*). Collection of additional cryo-EM micrographs of the M3/1–Fab complex followed by particle picking and two-dimensional class averaging revealed particles with features resembling an extended KS–acyltransferase (AT) didomain (fig. S8). Further reconstruction without imposed symmetry resulted in a 3.2-Å-resolution map that could be fitted with two M3 KS-AT didomains bound to a single Fab molecule (Fig. 2A, fig. S8, and table S1), but neither the ketoreductase (KR) and ACP domains of M1 nor the C-terminal TE domains could be resolved. The single Fab occupancy contrasts with the symmetric binding of two Fab heterodimers observed crystallographically (*15*), likely because of a bent conformation in the coiled-coil docking domain (detailed in fig. S9). A local resolution range of ~3.2 to 5 Å between the N-terminal docking domain and the AT-KR linker of M3/1 allowed for unambiguous assignment of the extended conformation to its KS-AT didomain (fig. S8). In regions beyond the

AT-KR linker, only two low-resolution lobes of density could be observed, which are assumed to be the flexible KR domains because of their domain connectivity (Fig. 2A). We speculated that the invisible KR-ACP-TE segment of this hybrid module might be disordered because of the lack of complementary interactions at its KS:KR interface.

On the basis of the above observations, we next purified DEBS M1 complexed to the same Fab. This module harbors a fully native KS-AT-KR-ACP segment fused to the N-terminal docking domain of M3 and the C-terminal TE domain (for improved expression and solubility). Single-particle cryo-EM analysis of the vitrified M1-Fab complex provided three structurally distinct and asymmetric maps with resolutions ranging from 3.2 to 4.1 Å, each with the expected Q-scores to reflect residue resolvability (figs. S10 to S12) (*24*). Each map reveals the KS-AT core bound to two Fab copies (fig. S10), as well as additional density for what appears to be one or both KRs. One map includes a clearly resolved

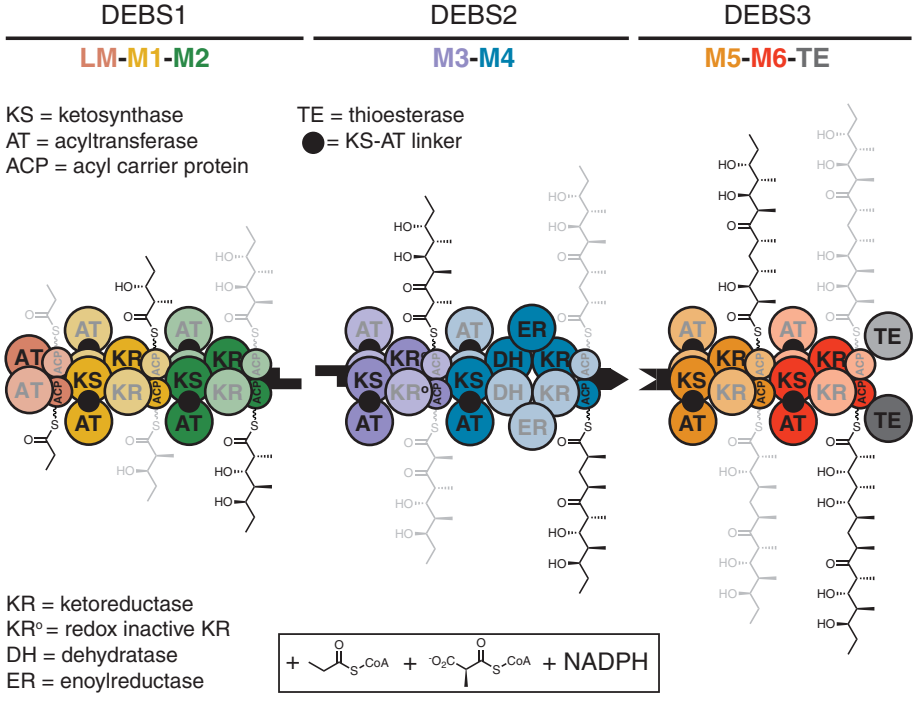

Fig. 1. Model for channeling of biosynthetic intermediates by the DEBS assembly line. DEBS includes three homodimeric polypeptides (DEBS 1 to 3) with a collective molecular mass of 2.1 MDa and harbors six elongation modules (M1 to M6) flanked by a loading module (LM) and a terminal TE domain. When provided propionyl-CoA (starter unit), (2*S*)-methylmalonyl-CoA (extender units), and NADPH, the assembly line synthesizes 6-deoxyerythronolide B, the macrocyclic aglycone of the antibiotic erythromycin. Two growing polyketide chains are synthesized in parallel by two sets of active sites of the homodimeric DEBS; individual monomeric copies of each module are distinguished by heavy and light shading. Earlier experiments established that translocation of the polyketide intermediate from one module to the next involves intrapolypeptide ACP→KS channeling, whereas polyketide chain elongation involves interpolypeptide KS→ACP channeling across the dimer interface (*5*). The cryo-EM structures solved in this work provide a clear mechanistic rationale for this observation. Shape-complementary black tabs at the end of each protein represent docking domains that facilitate intermodular polyketide translocation (*40*).

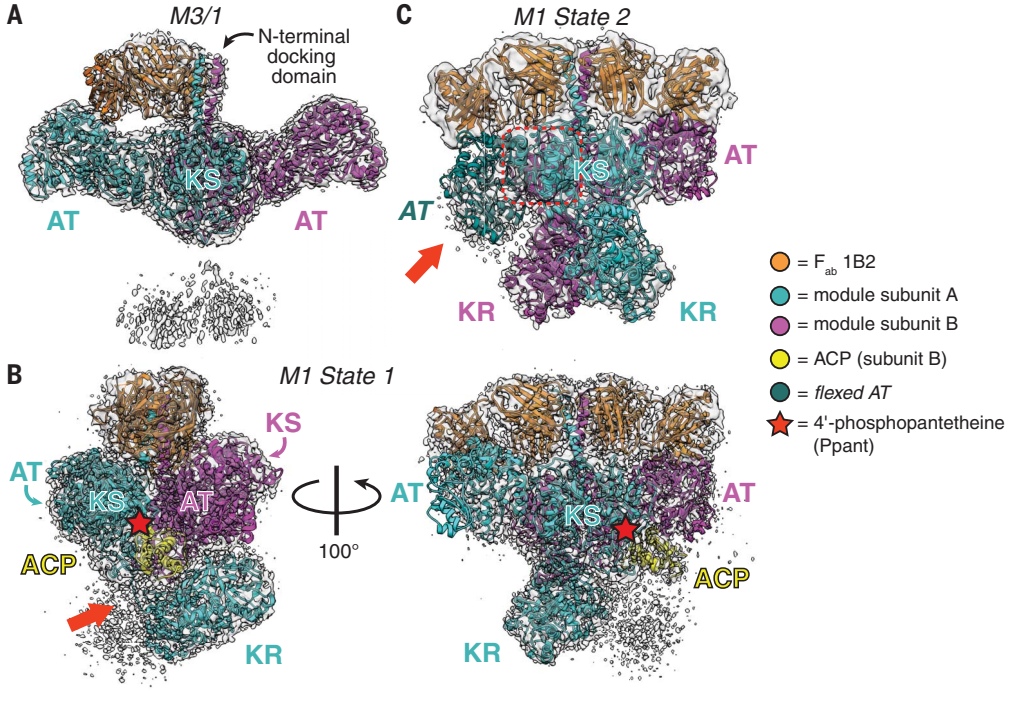

Fig. 2. Snapshots of three asymmetric cryo-EM structures. (**A**) The 3.2-Å-resolution structure of a hybrid module composed of domains from DEBS M3/1 (map threshold = 0.28). (**B** and **C**) Two distinct states of DEBS M1. (B) The 3.2-Å-resolution structure of *State 1* in which the P-pant cofactor (red star) of one ACP domain is bound in the KS active site of the other monomer (map threshold = 0.53). The red arrow highlights the resolved AT-KR linker (figs. S12, S13, and S14A and supplementary text). (C) The 4.1-Å-resolution structure of *State 2* featuring two symmetric KR domains in addition to an atypically flexed AT domain (red arrow). Dashed red box is the KS-AT linker that is not conformationally altered by AT flexing (fig. S17 and movie S1; map threshold = 0.35). Domain acronyms are defined in Fig. 1. Note that the color scheme (bottom) adopted for this figure is different from that of Fig. 1 because a different color palette was needed to clearly distinguish the module subunits, Fabs, and ACP.

ACP, although no features suggest a discernible TE domain.

The best-resolved map of the M1-Fab complex, obtained at 3.2-Å resolution and corresponding to one of the three classes, featured a single KR and a single ACP; this is hereafter referred to as the asymmetric *State 1*. Further model fitting and real-space refinement revealed an extended, homodimeric KS-AT core, albeit with reduced local resolution at the flanks of both AT domains, which may be altered relative to canonical KS-AT structures defined through x-ray crystallography (Fig. 2B, fig. S11, and table S1). The AT-KR linker could be fully traced to accurately assign the subunit to which the visible KR is attached (Fig. 2B; figs. S12, S13, and S14A; and supplementary text). This KR domain is buttressed by a patch of non-canonically structured KS residues (Asp75 to Arg86; Fig. 2B and fig. S14, A and B). Its orientation is rotated by ~90° compared with our previous low-resolution model of DEBS M3 (*17*). Interacting residue pairs of the KS:KR intermolecular interface could be accurately visualized (local resolution ~3.2 to 5 Å; Fig. 3, A and B, and figs. S11 and S14B), providing an unprecedented glimpse into quaternary structural interactions between the KS-AT catalytic core and the reductive segment of an assembly-line PKS module. Mapping of the sequences of 300 homologous PKS modules onto the structure of DEBS M1 indicated considerable diversity at this domain-domain interface (fig. S14C) (*25*). More detailed comparative analysis between the six elongation modules of DEBS and 12 additional modules drawn from the closest homologs of DEBS M1 revealed that the KS:KR interface is more conserved across orthologs of DEBS M1 than other DEBS modules (fig. S15), perhaps reflecting a fitness advantage to the conservation of this interface in modules with shared biosynthetic chemistry. This protein interface also revealed a pronounced electrostatic complementarity (fig. S15E), thereby offering a foothold into structure-based engineering of heterologous KS:KR interfaces. Although previous domain-swapping efforts have exploited variable interdomain linker regions to define heterologous junctions (*26*–*28*), no studies to our knowledge have attempted to modify domain-internal residues that comprise the KS:KR interface observed in our *State 1* structure.

Perhaps the most noteworthy feature of *State 1* is that one of the ACP domains is observed in the KS-AT cleft in a manner consistent with our previous model for polyketide elongation (*29*, *30*). Earlier mutational analysis identified loop 1 residues of the ACP as being the most important for elongation; the same residues comprise the chief ACP contacts in *State 1*. Interdomain interactions are observed between the ACP and both KS domains of the homodimer as well as the KS-AT linker (fig. S16). Closer inspection of the KS:ACP interface revealed a tunnel of continuous density between the modified Ser (S1449) of the ACP and KS catalytic Cys (C205) separated by ~16 Å, consistent with the 4′-phosphopantetheine (P-pant) cofactor of the ACP embedding into the KS active site (Fig. 3C and fig. S16). Modeling of the P-pant arm and its congruence with the density is supported by Q-score analysis (fig. S12A). In addition to C205, the P-pant thiol is in close proximity to other KS active site residues (i.e., H340, K373, and H378), consistent with placing a 2(*S*)-methylmalonyl extender unit favorably for catalysis. We therefore propose that *State 1* is descriptive of an asynchronously operating elongation mode of a homodimeric PKS module.

Another map, designated *State 2*, from the same M1-Fab particle dataset was resolved at 4.1-Å resolution and featured both KRs oriented symmetrically about the C_2 axis of the homodimeric module. This class was initially fitted from relevant portions of the *State 1* structure in addition to a second KR copy (Fig. 2C, figs. S10 and S11, and table S1). Subunit tracing in the *State 2* map favors a model in which the KRs interact with the KS of their own subunit, in contrast to the intermolecular KS:KR pairing observed in *State 1*. Thus, the reductive segment of an assembly-line PKS module must be capable of significant (~180°) C_2 rotational motions. Real-space refinement of the *State 2* model revealed another notable feature: One of the AT domains is flexed downward relative to the canonical crystallographic structure of the KS-AT core (Fig. 2C and fig. S17A). Unrestrained fitting suggests that the observed flexing of the AT domain hinges on two unstructured linkers, Thr551–Gln555 and Arg860–Ser864 (fig. S17A and movie S1) (*31*, *32*), although local resolution at the AT was reduced (fig. S11). This flexing occurs within the boundaries of the AT domain, leaving the KS-AT linker unaltered, a key distinction from the previously reported "arched" conformation of pikromycin synthase module 5 (fig. S17, A and B) (*6*, *7*). Furthermore, this flexing constricts the KS-AT cleft, thereby precluding the ability of the ACP domain to gain access to the KS active site as defined by *State 1* (fig. S18) and offering a clue into the structural basis for the experimentally observed gating of the KS (i.e., the turnstile mechanism) (*10*). Taking a reductionist, two-state-model approach, we therefore postulate that *State 2* is descriptive of the translocation and/or transacylation mode of a PKS module (fig. S1).

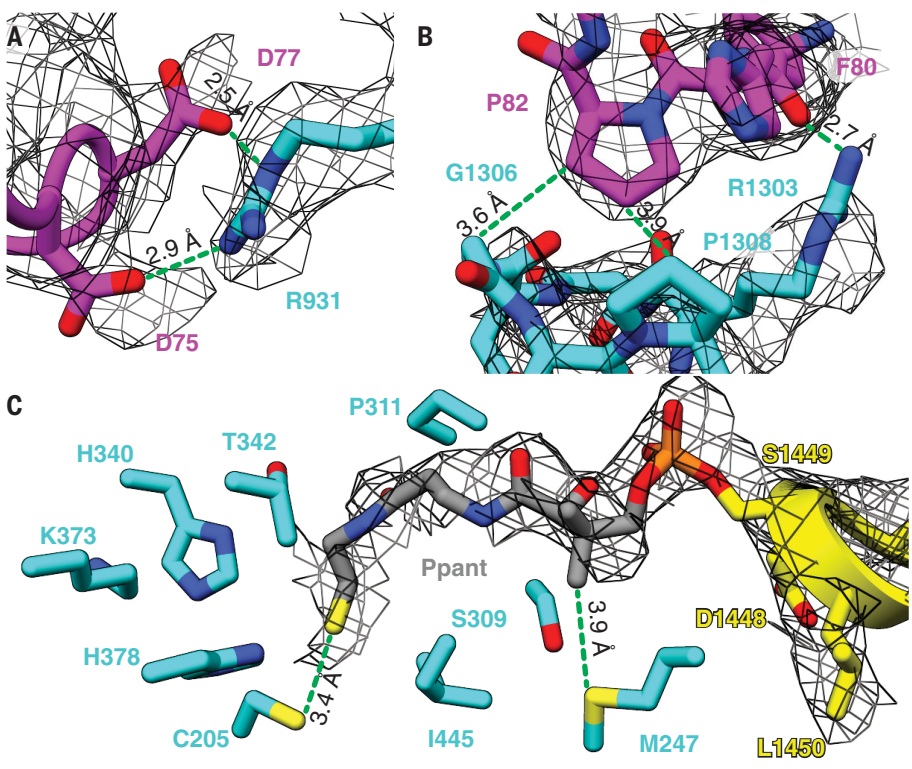

Fig. 3. The KS:KR interface and the P-pant arm of the ACP domain in the cryo-EM density map of *State 1* of DEBS M1. (**A** and **B**) Selected residues at the KS:KR interface. These residues are conserved in homologous PKS modules (fig. S15). (**C**) The P-pant arm is attached to Ser1449 of the ACP domain and extends to interact with Cys205 in the KS active site.

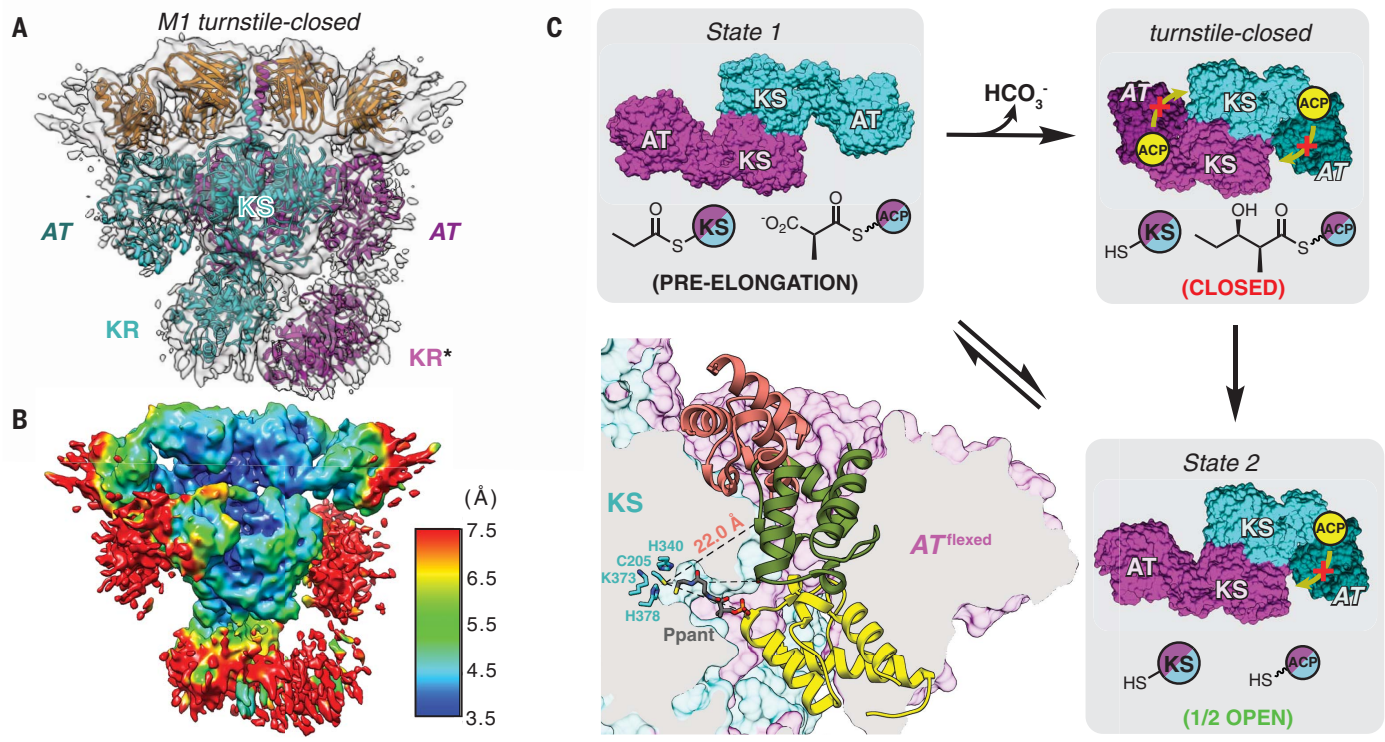

Fig. 4. Cryo-EM analysis of DEBS M1 in its *turnstile-closed* state. (**A**) The 4.3-Å-resolution cryo-EM structure of M1 in its post-elongation (*turnstile-closed*) state was solved, as described in the text (map threshold = 0.26). *The KR domain of subunit B (magenta) has been modeled here, although it is absent from the deposited coordinates because of orientation ambiguity and reduced local resolution [~7.5 Å in (B); PDB 7M7J]. (**B**) Resolution map for the structure in (A) (map threshold = 0.26). (**C**) Bottom left panel, ACP inaccessibility of the KS active site in this state. Accessibility of the cleft resulting from AT flexing was evaluated using the KS-ACP interaction pose observed in *State 1* (yellow ACP) as well as two prior models for KS-ACP interaction during intermodular polyketide translocation (*6*, *7*), (*29*, *30*) (salmon and green ACPs, respectively). Although the yellow and green poses are disfavored for steric reasons, the P-pant arm of the salmon pose is insufficiently long to access the KS active site (see fig. S23 for details). Remaining panels show a model for asymmetric turnstile closing of M1. Upon chain elongation, the pre-elongation state (*State 1*) undergoes a conformational change into its *turnstile-closed* state (A) to occlude the KS active site from an upstream or intramodular ACP, shown in yellow (movie S3). The duration of the *turnstile-closed* state is long enough to allow the ACP-bound diketide to undergo KR-catalyzed reduction and translocation to the downstream module, after which one catalytic subunit of the module returns to its translocation-competent state (*State 2*). Note that only the KS and AT catalytic domains are shown for clarity, and the KS and ACP acylation states are depicted for both modular subunits behaving equivalently but asynchronously.

Although the associated map of the *State 1* structure does not resolve the KR-ACP linker with sufficient clarity to identify the subunit to which the structurally defined ACP is attached, we predicted it would be attached to subunit B (colored magenta in Fig. 2B) in accordance with earlier evidence that polyketide chain elongation occurs across subunits (*5*). To resolve this ambiguity, we further classified the M1 dataset using heterogeneous refinement to identify candidate classes with better structural resolution near the N terminus of the ACP domain. One class average meeting this criterion was selected and further processed to obtain a 4.1-Å-resolution map of M1. This model, hereby designated as *State 1′*, is reminiscent of *State 1* but reveals additional density corresponding to the second KR (figs. S10 to S12 and S19 and table S1). Although the KR and ACP domains are not as well resolved, a continuous region of density can be traced between these two domains, allowing inference of the subunit connectivity of the single ACP domain observed in the higher-resolution *State 1* structure (Fig. 2B and fig. S19); in turn, this structural model verifies that polyketide elongation occurs intermolecularly (*5*). As a corollary, the KR connected to the ACP must undergo significant rotational and translational motion relative to its position in *State 2* to position the ACP into its KS-AT cleft for elongation (fig. S19). These findings reinforce the notion that the lower torso region of the module (i.e., C-terminal to the AT) exhibits a high degree of conformational flexibility.

Integrating the above structural data, a model for the catalytic cycle of DEBS M1 emerges with four key features. First, the transition from its translocation and/or transacylation state (*State 2*) to its elongation state (*State 1*) requires the flexible KR domain of the homodimeric module to undergo rotational and translational motion. Second, chain elongation requires intermolecular docking of the ACP domain from one subunit onto the KS domain from the other subunit. Third, chain elongation is asynchronously catalyzed by the two KS-ACP pairs of the homodimeric module. Finally, post-elongation "turnstile" closing of M1 involves a conformational change in the KS-AT core that transiently occludes the KS active site from the ACP domain of the upstream loading module to allow the newly formed ACP-bound diketide to undergo β-ketoreduction and be translocated to M2.

To test this model, we prepared DEBS M1 in its diketide-bound form (fig. S1). To prevent chain release, the construct lacked a C-terminal TE domain (see the supplementary materials for details). The resulting protein was complexed with Fab 1B2, incubated with its native substrates for a sufficient duration

to complete one catalytic cycle, promptly vitrified, and subjected to cryo-EM analysis. The resulting 4.3-Å-resolution cryo-EM map of the diketide-linked module (Fig. 4A, figs. S20 and S21, and table S1) revealed a distinct structural change in which both AT domains resided in a flexed orientation analogous to the flexed AT observed in *State 2* of M1 (Fig. 2C).

As before, the conformation of the flexed ATs in the product-bound state is accompanied by an ~8000-Å^3 reduction in the KS-AT cleft volumes, thereby blocking accessibility to acyl-ACP substrates for repeated elongation (fig. S18). Thus, the product-bound state appears to provide a structural rationale for turnstile closing, albeit with modest support from the poorly resolved AT domains (~7.5 Å, Fig. 4B; see fig. S22 and movie S2 for visualization of the map at various thresholds and movie S3 for visualization of turnstile closing). On the basis of this observation, we have therefore assigned the product-bound structure of M1 as the *turnstile-closed* state. To address whether the *turnstile-closed* state can support intermodular polyketide translocation, we evaluated two previous models for ACP binding during translocation (Fig. 4C and described in fig. S23). The results from model superpositions are consistent with a KS-AT cleft that is too constricted for ACP entry during translocation, providing an additional layer of support for the structural basis of turnstile closing. The catalytic cycle is summarized in Fig. 4C, and its conformational dynamic aspects are detailed in fig. S24.

At present, hundreds of assembly-line PKSs have been functionally annotated (*33*), and in silico prediction tools (*34*–*36*) are gaining widespread acceptance as more systems are sequenced and characterized (*37*). Although the elementary reactions of substrate loading and elongation are conserved across each assembly line, frequent reports that defy the DEBS paradigm continue to expand our sense of the enzymology that is possible both on (*38*) and off (*39*) the assembly line. Despite these advances, the fundamental question of how assembly-line PKSs coordinate their vectorial biosynthetic chemistry across multiple modules in sequence remains unanswered. A satisfactory answer will require high-resolution spatiotemporal information on PKS modular dynamics.

REFERENCES AND NOTES

1. D. J. Newman, G. M. Cragg, *J. Nat. Prod.* **83**, 770–803 (2020).
2. H. A. Kirst, *J. Antibiot. (Tokyo)* **63**, 101–111 (2010).
3. T. Robbins, Y.-C. Liu, D. E. Cane, C. Khosla, *Curr. Opin. Struct. Biol.* **41**, 10–18 (2016).
4. C. Khosla, Y. Tang, A. Y. Chen, N. A. Schnarr, D. E. Cane, *Annu. Rev. Biochem.* **76**, 195–221 (2007).
5. C. M. Kao, R. Pieper, D. E. Cane, C. Khosla, *Biochemistry* **35**, 12363–12368 (1996).
6. S. Dutta *et al*., *Nature* **510**, 512–517 (2014).
7. J. R. Whicher *et al*., *Nature* **510**, 560–564 (2014).
8. M. A. Skiba *et al*., *ACS Chem. Biol.* **13**, 1640–1650 (2018).
9. J. Wang *et al*., *Nat. Commun.* **12**, 867 (2021).
10. B. Lowry, X. Li, T. Robbins, D. E. Cane, C. Khosla, *ACS Cent. Sci.* **2**, 14–20 (2016).
11. A. Chari *et al*., *Nat. Methods* **12**, 859–865 (2015).
12. R. S. Gokhale, S. Y. Tsuji, D. E. Cane, C. Khosla, *Science* **284**, 482–485 (1999).
13. A. Y. Chen, N. A. Schnarr, C.-Y. Kim, D. E. Cane, C. Khosla, *J. Am. Chem. Soc.* **128**, 3067–3074 (2006).
14. B. Lowry *et al*., *J. Am. Chem. Soc.* **135**, 16809–16812 (2013).
15. X. Li *et al*., *J. Am. Chem. Soc.* **140**, 6518–6521 (2018).
16. Y. Tang, A. Y. Chen, C.-Y. Kim, D. E. Cane, C. Khosla, *Chem. Biol.* **14**, 931–943 (2007).
17. A. L. Edwards, T. Matsui, T. M. Weiss, C. Khosla, *J. Mol. Biol.* **426**, 2229–2245 (2014).
18. S. C. Tsai *et al*., *Proc. Natl. Acad. Sci. U.S.A.* **98**, 14808–14813 (2001).
19. L. Griffin, A. Lawson, *Clin. Exp. Immunol.* **165**, 285–291 (2011).
20. S. Wu *et al*., *Structure* **20**, 582–592 (2012).
21. D. P. Cogan *et al*., *J. Am. Chem. Soc.* **142**, 14933–14939 (2020).
22. A. T. Keatinge-Clay, R. M. Stroud, *Structure* **14**, 737–748 (2006).
23. S. R. Bagde, I. I. Mathews, J. C. Fromme, C.-Y. Kim, *Science* **374**, 723–729 (2021).
24. G. Pintilie *et al*., *Nat. Methods* **17**, 328–334 (2020).
25. H. Ashkenazy *et al*., *Nucleic Acids Res.* **44**, W344–W350 (2016).
26. M. Klaus, M. Grininger, *Nat. Prod. Rep.* **35**, 1070–1081 (2018).
27. S. Yuzawa *et al*., *ACS Synth. Biol.* **6**, 139–147 (2017).
28. A. Hagen *et al*., *ACS Synth. Biol.* **5**, 21–27 (2016).
29. S. Kapur, A. Y. Chen, D. E. Cane, C. Khosla, *Proc. Natl. Acad. Sci. U.S.A.* **107**, 22066–22071 (2010).
30. S. Kapur *et al*., *Proc. Natl. Acad. Sci. U.S.A.* **109**, 4110–4115 (2012).
31. L. G. Trabuco, E. Villa, K. Mitra, J. Frank, K. Schulten, *Structure* **16**, 673–683 (2008).
32. L. G. Trabuco, E. Villa, E. Schreiner, C. B. Harrison, K. Schulten, *Methods* **49**, 174–180 (2009).
33. S. A. Kautsar *et al*., *Nucleic Acids Res.* **48** (D1), D454–D458 (2020).
34. K. Blin *et al*., *Nucleic Acids Res.* **47** (W1), W81–W87 (2019).
35. P. Cimermancic *et al*., *Cell* **158**, 412–421 (2014).
36. M. A. Skinnider, N. J. Merwin, C. W. Johnston, N. A. Magarvey, *Nucleic Acids Res.* **45** (W1), W49–W54 (2017).
37. A. Nivina, K. P. Yuet, J. Hsu, C. Khosla, *Chem. Rev.* **119**, 12524–12547 (2019).
38. A. T. Keatinge-Clay, *Chem. Rev.* **117**, 5334–5366 (2017).
39. E. J. N. Helfrich, J. Piel, *Nat. Prod. Rep.* **33**, 231–316 (2016).
40. R. W. Broadhurst, D. Nietlispach, M. P. Wheatcroft, P. F. Leadlay, K. J. Weissman, *Chem. Biol.* **10**, 723–731 (2003).

ACKNOWLEDGMENTS

We thank J. Perrino and D.-H. Chen (Stanford University) for assistance with initial negative-stain and cryo-EM condition screening. **Funding:** This work was supported by the National Institutes of Health (grants R01GM087934 and R35GM141799 to C.K.; grant F32GM136039 to D.P.C.; and grants R01GM079429, P41GM103832, S10OD021600, and U24GM129541 to W.C.).
Author contributions: C.K., W.C., D.P.C., and K.Z. conceived of the experimental design and project aims. C.S.C. provided key reagents and advice on best practices for their utilization. D.P.C. and K.Z. collected all of the non–cryo-EM experimental data, which were analyzed by all authors. K.Z., X.L., and S.-H.R. conducted preliminary experiments that informed the experiments described in this manuscript. K.Z. and S.L. performed the cryo-EM data collection and processing steps that led to the final deposited cryo-EM maps. K.Z. and D.P.C. refined the models. G.D.P. conducted the Q-score analysis and generated movies S2 and S3. C.K., W.C., and C.S.C. supervised all experiments. D.P.C. and C.K. wrote the initial manuscript, which was then revised and edited by all authors. **Competing interests:** The authors declare no competing financial interests. **Data and materials availability:** All cryo-EM maps and atomic coordinates have been deposited in the Protein Data Bank under accession codes 7M7E, 7M7F, 7M7G, 7M7H, 7M7I, and 7M7J and in the Electron Microscopy Data Bank under accession codes EMD-23710, EMD-23711, EMD-23712, EMD-23713, EMD-23714, and EMD-23715. All other data are present in the main text or the supporting materials.

SUPPLEMENTARY MATERIALS

science.org/doi/10.1126/science.abi8358
Materials and Methods
Supplementary Text
Figs. S1 to S24
Tables S1 to S3
References (*41*–*69*)
Movies S1 to S3
MDAR Reproducibility Checklist

View/request a protocol for this paper from *Bio-protocol*.

2 April 2021; accepted 9 September 2021
10.1126/science.abi8358

Mapping the catalytic conformations of an assembly-line polyketide synthase module

Dillon P. CoganKaiming ZhangXiuyuan LiShanshan LiGrigore D. PintilieSoung-Hun RohCharles S. CraikWah ChiuChaitan Khosla

Science, 374 (6568), • DOI: 10.1126/science.abi8358

Big molecules build small

Actinomycete bacteria are prolific producers of bioactive small molecules such as polyketide antibiotics. These molecules are built by the addition of short carbon units to a growing, protein-tethered chain, either iteratively as in fatty acid synthesis or in a modular fashion by a hand-off from one distinct enzyme complex to the next. Bagde *et al*. and Cogan *et al*. report structures of polyketide synthase modules in action, taking advantage of antibody stabilization of one of the domains. Both groups visualized multiple conformational states and an asymmetric arrangement of domains, providing insight into how these molecular assembly machines transfer substrates from one active site to another. —MAF